J. Fluid Mech. (1983), *vol.* 130, *pp.* 377–395
Printed in Great Britain

Numerical study of secondary flows and roll-cell instabilities in rotating channel flow

By CHARLES G. SPEZIALE AND SIVAGNANAM THANGAM
Stevens Institute of Technology, Hoboken, NJ 07030

(Received 16 September 1982 and in revised form 7 January 1983)

A numerical study is conducted on the pressure-driven laminar flow of an incompressible viscous fluid through a rectangular channel subjected to a spanwise rotation. The full nonlinear time-dependent Navier–Stokes equations are solved by a finite-difference technique for various rotation rates and Reynolds numbers in the laminar regime. At weak rotation rates, a double-vortex secondary flow appears in the transverse planes of the channel. For more rapid rotation rates, an instability occurs in the form of longitudinal roll cells in the interior of the channel. Further increases in the rotation rate leads to a restabilization of the flow to a Taylor–Proudman regime. It is found that the roll-cell and Taylor–Proudman regimes lead to a substantial distortion of the axial-velocity profiles. The specific numerical results obtained are shown to be in excellent agreement with previously obtained experimental measurements and theoretical predictions.

1. Introduction

During the past decade, a considerable amount of research has been conducted on laminar secondary flows and roll-cell instabilities in pressure-driven channel flow subjected to a spanwise rotation. Hart (1971) was the first to conduct detailed measurements of such a flow for a variety of rotation rates. These measurements were carried out with water (to allow for dye visualization) in a rectangular channel with an aspect ratio $H/D \approx 7$ for weak to relatively rapid rotation rates (see figure 1). The results of these experiments clearly demonstrated the existence of three regimes in rotating channel flow. At weak rotation rates there is a double-vortex secondary flow; at intermediate rotation rates there is an instability in the form of longitudinal roll cells; and at more rapid rotation rates there is a restabilization of the flow to a Taylor–Proudman regime where the axial velocity profiles do not vary along the direction of the axis of rotation in the interior of the channel. Hart also carried out a theoretical analysis of the secondary flow structure for the weak-rotation case and a linear stability analysis for the onset of roll cells in rotating plane Poiseuille flow (i.e. the limiting case of a rectangular channel with an infinite aspect ratio as shown in figure 2). The results of these analyses were in general agreement with the experimental data that was obtained. Furthermore, Hart demonstrated that the general stability problem for rotating Poiseuille flow is exactly analogous (i.e. valid for the general time-dependent nonlinear case) to the stability problem of a temperature-stratified fluid with the appropriate stratification.

Lezius & Johnston (1976) conducted a more detailed theoretical analysis of laminar roll-cell instabilities in rotating channel flow. Their investigations included a linear stability analysis for the onset of laminar roll cells in rotating plane Poiseuille flow. This was accomplished by a finite-difference method (see Lezius 1975), as opposed

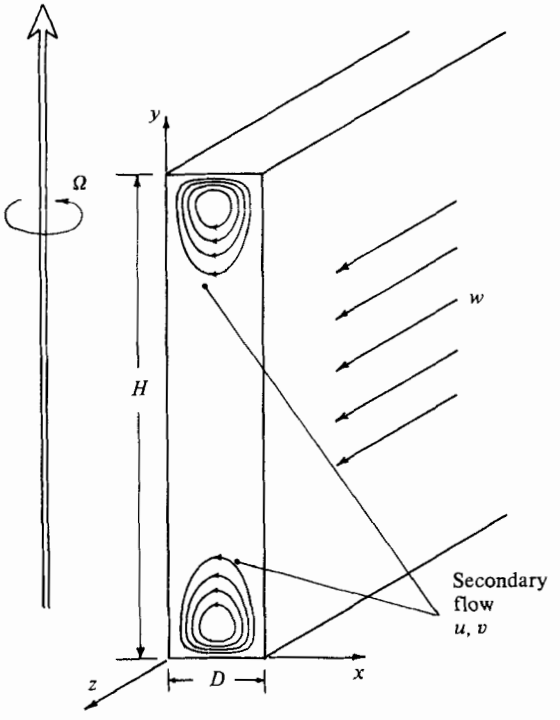

FIGURE 1

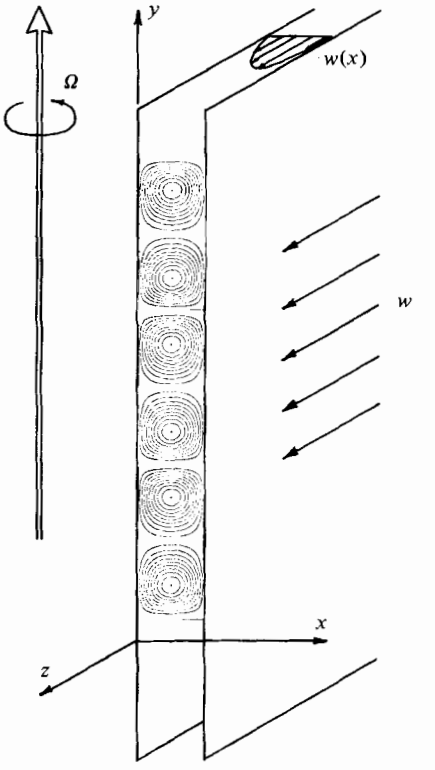

FIGURE 2

FIGURE 1. Secondary flow in a rectangular channel subjected to a weak spanwise rotation (after Hart 1971).

FIGURE 2. Roll-cell instabilities in plane Poiseuille flow subjected to a spanwise rotation (after Lezius & Johnston 1976).

to the Galerkin method which was used by Hart. The specific results obtained indicated that the critical disturbance occurs at a Reynolds number $Re = 88.53$ and a rotation number $Ro = 0.5$. However, for higher Reynolds numbers, they found that unstable conditions can exist for $0 < Ro < 3$. In general, these results predicted flow instability at somewhat lower Reynolds numbers for a given rotation rate than the results of Hart. Lezius & Johnston also conducted a linear stability analysis for the onset of roll-cell instabilities in turbulent plane Poiseuille flow subjected to a spanwise rotation. Despite the fact that the analysis was linear and involved turbulence modelling, the results obtained were nevertheless in excellent agreement with experiments (see Johnston, Halleen & Lezius 1972).

In the present paper we will present a detailed numerical study of rotating laminar channel flow in order to gain a more complete understanding of the various flow regimes that occur. The full nonlinear Navier–Stokes equations will be solved by a finite-difference method that was used in Speziale (1982) to analyse flow in a low-aspect-ratio rotating rectangular duct. Particular emphasis will be placed on the examination of roll-cell instabilities and the restabilization of the flow to a Taylor–Proudman regime in a rotating rectangular channel with an aspect ratio $H/D = 8$. Although there has been a considerable amount of research on roll-cell instabilities

as discussed above, none of this work consisted of a solution of the full nonlinear equations of motion with the inclusion of the end effects of boundaries (i.e. a finite-aspect-ratio channel). These considerations are important for a more complete understanding of this phenomenon in real physical systems. We will also make a detailed study of the secondary-flow structure in the Taylor–Proudman regime. To the best of our knowledge, no calculations have been performed to date on this regime in a large-aspect-ratio channel. In fact, even the experimental observations of this regime are somewhat incomplete (e.g. there are no published experimental observations of the secondary-flow streamlines in the Taylor–Proudman regime). Furthermore, unlike in all of the previous studies, we will calculate the time evolution of rotating channel flow to gain further insight into the stabilizing and destabilizing mechanisms that occur. Comparisons with existing experimental data and the prospects for future research will be discussed in later sections.

2. Formulation of the physical problem

The physical problem to be considered is that of the laminar pressure-driven flow of an incompressible viscous fluid through a straight rectangular channel subjected to a steady spanwise rotation Ω (see figure 1). The axial pressure gradient $\partial P/\partial z = -G$ is constant (where P is the modified pressure, which includes the gravitational and centrifugal force potentials) and is maintained by external means. Here, the channel is sufficiently long so that there exists an interior portion where end effects can be suppressed and the flow properties are independent of the axial coordinate z. In the absence of rotations, the fully developed velocity field $\boldsymbol{v}$ is of the unidirectional form

$$\boldsymbol{v} = w(x,y)\,\boldsymbol{k}, \tag{2.1}$$

where w is determined from the Poisson equation (cf. Batchelor 1967)

$$\nabla^2 w = -G/\mu, \tag{2.2}$$

and μ is the shear viscosity of the fluid. Equation (2.2) is solved subject to the no-slip condition that w vanishes on the walls of channel. This yields the classical quasiparabolic velocity profile.

For non-zero rotation rates, the fully developed velocity field is three-dimensional relative to an observer who rotates with the channel (cf. Hart 1971), i.e. $\boldsymbol{v}$ is of the form

$$\boldsymbol{v} = u(x,y)\,\boldsymbol{i} + v(x,y)\boldsymbol{j} + w(x,y)\,\boldsymbol{k}, \tag{2.3}$$

where u and v constitute the secondary flow. The velocity vector $\boldsymbol{v}$ is a solution of the Navier–Stokes equations and the continuity equation, which, relative to an observer who is rotating with the channel (i.e. at an angular velocity $\boldsymbol{\Omega} = \Omega\boldsymbol{j}$), take the form

$$\frac{\partial u}{\partial t} + u\frac{\partial u}{\partial x} + v\frac{\partial u}{\partial y} = -\frac{1}{\rho}\frac{\partial P}{\partial x} + \nu\nabla^2 u - 2\Omega w, \tag{2.4}$$

$$\frac{\partial v}{\partial t} + u\frac{\partial v}{\partial x} + v\frac{\partial v}{\partial y} = -\frac{1}{\rho}\frac{\partial P}{\partial y} + \nu\nabla^2 v, \tag{2.5}$$

$$\frac{\partial w}{\partial t} + u\frac{\partial w}{\partial x} + v\frac{\partial w}{\partial y} = \frac{G}{\rho} + \nu\nabla^2 w + 2\Omega u, \tag{2.6}$$

$$\frac{\partial u}{\partial x} + \frac{\partial v}{\partial y} = 0, \tag{2.7}$$

where P is the modified pressure, ρ is the density of the fluid, $\nu \equiv \mu/\rho$ is the kinematic viscosity, and ∇^2 is the two-dimensional Laplacian, i.e.

$$\nabla^2 = \frac{\partial^2}{\partial x^2} + \frac{\partial^2}{\partial y^2}. \tag{2.8}$$

Of course, in formulating (2.4)–(2.7) we have made use of the fact that the velocity field is independent of the axial coordinate z. Furthermore, the transient form of the Navier–Stokes equations are given since we intend to study the time evolution of the flow.

As a result of the simplified form of the continuity equation (2.7), there exists a stream function ψ for the secondary flow so that

$$u = -\frac{\partial \psi}{\partial y}, \quad v = \frac{\partial \psi}{\partial x}, \tag{2.9}$$

where ψ is a solution of the Poisson equation

$$\nabla^2 \psi = \omega. \tag{2.10}$$

In (2.10)

$$\omega \equiv \omega_z = \frac{\partial v}{\partial x} - \frac{\partial u}{\partial y} \tag{2.11}$$

is the axial component of the vorticity, which is determined from the z-component of the vorticity-transport equation given by

$$\frac{\partial \omega}{\partial t} + u\frac{\partial \omega}{\partial x} + v\frac{\partial \omega}{\partial y} = \nu \nabla^2 \omega + 2\Omega \frac{\partial w}{\partial y}. \tag{2.12}$$

As a consequence of (2.10) it is quite clear that secondary flows result from a non-zero axial vorticity ω. It is, therefore, obvious that the Coriolis term $2\Omega\, \partial w/\partial y$ (which serves an as axial-vorticity source term in (2.12)) is the driving mechanism for the creation of secondary flows in a rotating rectangular channel.

A modified vorticity–stream-function approach was chosen for this numerical study. More specifically, the following system of equations will be solved numerically:

$$\frac{\partial w}{\partial t} + u\frac{\partial w}{\partial x} + v\frac{\partial w}{\partial y} = \frac{G}{\rho} + \nu \nabla^2 w + 2\Omega u, \tag{2.13a}$$

$$\frac{\partial \omega}{\partial t} + u\frac{\partial \omega}{\partial x} + v\frac{\partial \omega}{\partial y} = \nu \nabla^2 \omega + 2\Omega \frac{\partial w}{\partial y}, \tag{2.13b}$$

$$\nabla^2 \psi = \omega, \tag{2.13c}$$

$$u = -\frac{\partial \psi}{\partial y}, \quad v = \frac{\partial \psi}{\partial x}. \tag{2.13d}$$

This coupled system of nonlinear partial differential equations (2.13) must be solved subject to the boundary conditions

$$u = 0, \quad v = 0, \quad w = 0, \quad \psi = 0$$

on the walls of the channel. The boundary conditions on the axial vorticity ω can be derived by a Taylor expansion of (2.13c) near the walls of the channel (see Speziale 1982). The initial-value problem to be considered is that of the spin-up of an initially

fully developed channel flow. Here, the angular velocity Ω is impulsively applied at time $t = 0$ with

$$u = 0, \quad v = 0, \quad w = w_{\mathrm{i}}, \quad \omega = 0, \quad \psi = 0, \tag{2.14}$$

where w_{i} is the classical quasiparabolic velocity profile obtained from (2.2). This constitutes the way the experiments are usually conducted on rotating channel flow (cf. Hart 1971).

The system of equations (2.13*a–d*) will be solved by an explicit finite-difference approach that was discussed in detail and used by Speziale (1982). In this approach, the convective terms and viscous terms in (2.13*a*, *b*) are respectively formulated by Arakawa's scheme and the DuFort–Frankel scheme (cf. Roach 1972). The Coriolis terms are centred in time. The Poisson equation for the stream function (2.13*c*) is formulated in its standard second-order-accurate finite-difference form by a high-speed Poisson solver that employs cyclic reduction (see Buneman 1969). Equation (2.13*d*), i.e. the secondary-flow velocity–stream-function relations, are central-differenced. This finite-difference formulation, in its totality, constitutes a second-order-accurate conservative difference scheme which has no boundary-condition problems. In addition to being linearly stable, it is not subject to nonlinear instabilities that arise from aliasing errors, since all aliasing errors are bounded.

The calculations were carried out in a rectangular channel with an aspect ratio $H/D = 8$ which was discretized into a 16×128 grid. The physical properties chosen were that for water (at room temperature) flowing in a channel with a width $D = 1.92$ in. and height $H = 15.36$ in. (these dimensions correspond to uniform grid lengths Δx, $\Delta y = 0.01$ ft). For this case, it should be noted that $\nu = 1.1 \times 10^{-5}$ ft^2/s and $\rho = 1.936$ slugs/ft^3. At this point we will introduce the following dimensionless numbers:

$$Re = \frac{W_0 D}{\nu}, \quad Ro = \frac{\Omega D}{W_0}, \quad E = \frac{\nu}{2\Omega D^2}, \tag{2.15}$$

which are respectively the Reynolds number, the rotation number and the Ekman number (W_0 is the integrated average axial velocity). These particular dimensionless numbers will be utilized for the comparisons with the experiments of Hart (1971) and Lezius & Johnston (1976). Since we were interested in examining the effect of a continuous increase in angular velocity for a fixed physical pressure gradient, there was no advantage to be gained by non-dimensionalizing the equations of motion *a priori*.

Computations were conducted in the laminar regime for a variety of Reynolds numbers and rotation numbers, mostly in the ranges

$$0 < Re < 500, \quad 10^{-4} < Ro < 3, \tag{2.16}$$

for which a considerable amount of experimental data were available for comparisons. These calculations required from 30 min to 1 hour on a DEC System-10 computer, with the lower time amount corresponding to the case where the secondary flow is weak. Since, from a localized linear stability analysis, we must have the time step Δt satisfy the constraint (cf. Roach 1972)

$$\Delta t \leqslant \left[2\nu \left(\frac{1}{\Delta x^2} + \frac{1}{\Delta y^2} \right) + \frac{|u|_{\max}}{\Delta x} + \frac{|v|_{\max}}{\Delta y} \right]^{-1}, \tag{2.17}$$

the cases with a stronger secondary flow (i.e. with a faster rotation rate) require a larger number of iterations for convergence.

In §3 we will examine the numerical results obtained in complete detail.

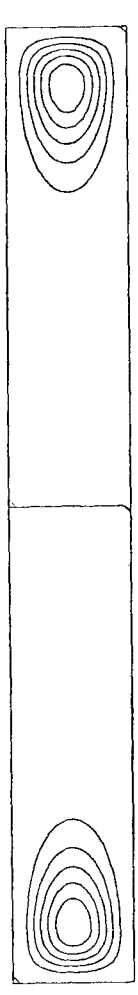

FIGURE 3

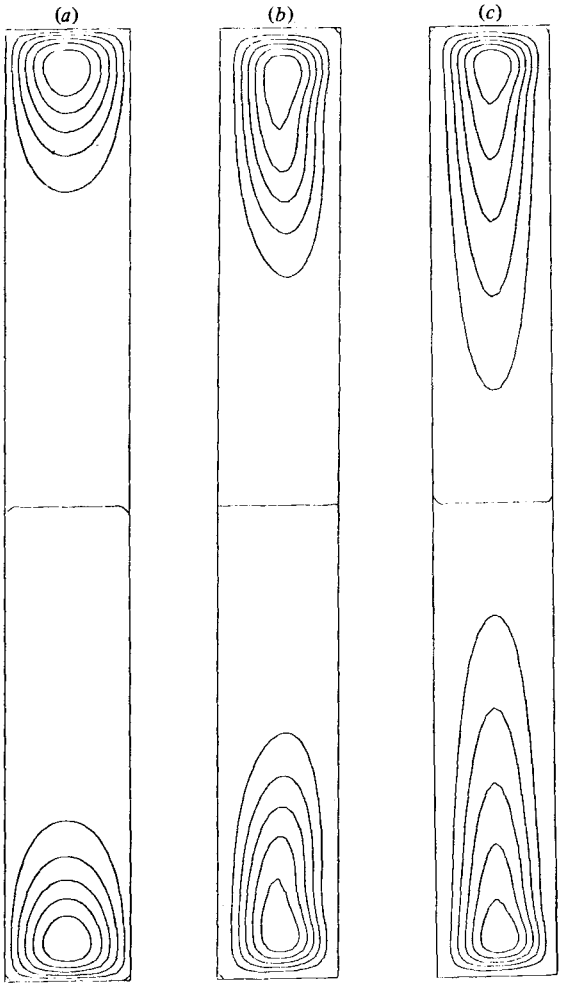

FIGURE 4

FIGURE 3. Computer-generated fully developed secondary-flow streamlines in an 8×1 channel; $Re = 80.4$, $Ro = 2.9 \times 10^{-4}$ ($\Omega = 10^{-5}$ rad/s, $G = 6 \times 10^{-5}$ lb/ft^3).

FIGURE 4. Computer-generated secondary-flow streamlines in an 8×1 channel; $Re = 107$, $Ro = 0.5$ ($\Omega = 0.023$ rad/s, $G = 8.6 \times 10^{-5}$ lb/ft^3): (*a*) $t = 1$ s; (*b*) 75 s; (*c*) fully developed.

3. Numerical results and comparisons with experiments

Initially we conducted computations for the weak-rotation case at various Reynolds numbers in the laminar regime. These results clearly demonstrated the existence of a double-vortex secondary-flow structure where each vortex, which has a lengthscale of the order of the width of the channel, is somewhat compressed against the wall of the channel to which it is adjacent. A computer-generated contour map of the fully developed secondary-flow streamlines for $Re = 80.4$ and $Ro = 2.9 \times 10^{-4}$ ($\Omega = 10^{-5}$ rad/s) is shown in figure 3, which illustrates these effects and is in qualitative agreement with the calculations of Hart (1971). In all of the contour maps that will be shown, the uppermost vortex rotates in the clockwise direction while the vortices below counter-rotate.

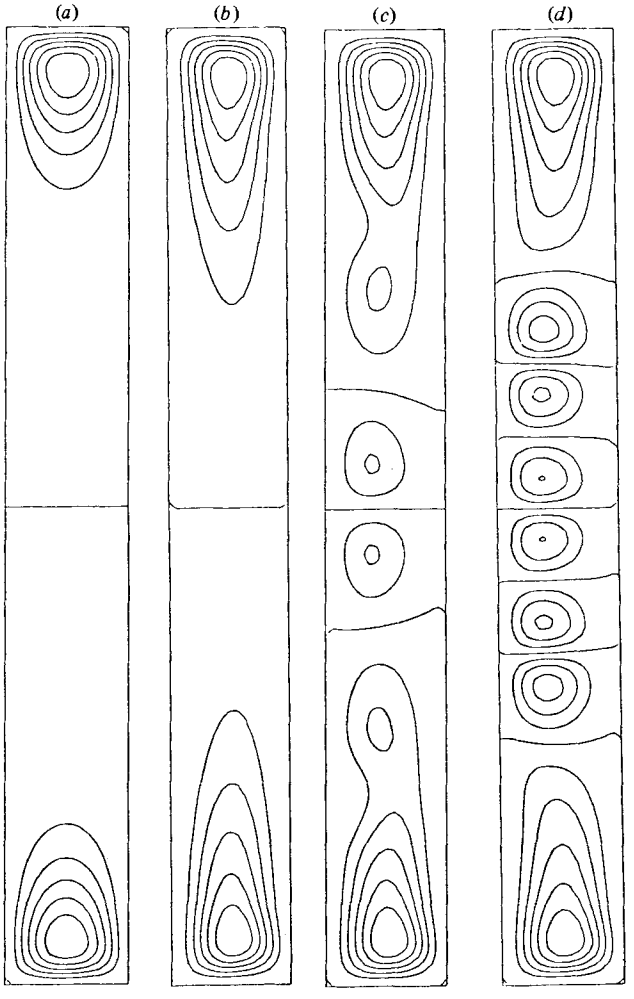

FIGURE 5. Computer-generated secondary-flow streamlines in an 8×1 channel; $Re = 248$, $Ro = 0.047$ ($\Omega = 0.005$ rad/s, $G = 2 \times 10^{-4}$ lb/ft^3): (*a*) $t = 10$ s; (*b*) 500 s; (*c*) 1600 s; (*d*) fully developed.

As the rotation rate is increased further, the secondary-flow vortices begin to stretch into the interior of the channel. An example of this phenomenon is shown in figure 4 for $Re = 107$ and $Ro = 0.5$. At this point, a small increase in the rotation rate leads to the onset of an instability in the form of longitudinal roll cells. It should be noted that it has only been proven rigorously that roll-cell solutions constitute an instability (i.e. a change to a higher-mode solution) for the case of rotating plane Poiseuille flow (see figure 2). This is easy to see, since for the case where $H/D \rightarrow \infty$, (2.13*a–d*) has the steady-state solution

$$w = w_c(x), \quad u = 0, \quad v = 0, \quad \omega = 0 \tag{3.1}$$

(where $w_c(x)$ is the classical parabolic velocity profile) for *all* values of Re and Ro. However, as shown in the linear stability analyses of Hart (1971) and Lezius & Johnston (1976), the unidirectional solution (3.1) becomes unstable in the presence of small disturbances when the Reynolds number exceeds a critical value for a certain

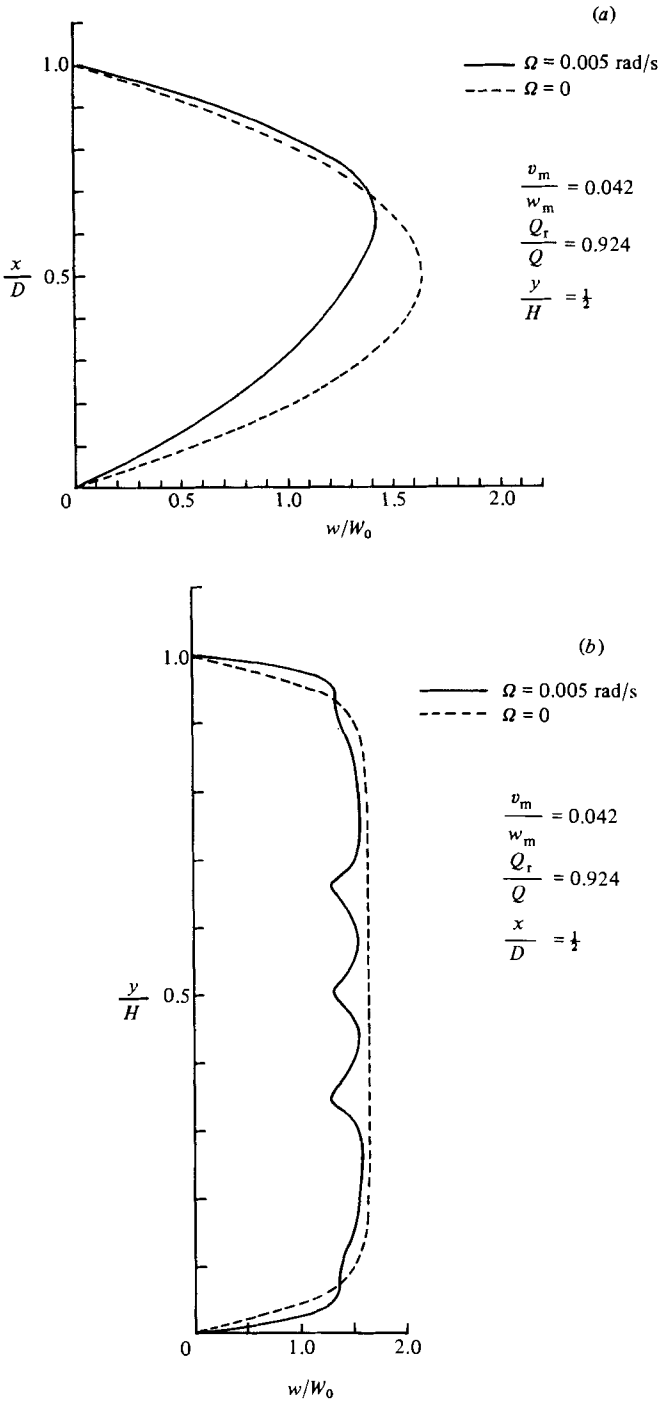

FIGURE 6. Axial-velocity profiles in an 8×1 channel; $Re = 248$, $Ro = 0.047$ ($\Omega = 0.005$ rad/s, $G = 2 \times 10^{-4}$ lb/ft^3): (*a*) along the horizontal centreline of the channel; (*b*) along the vertical centreline of the channel.

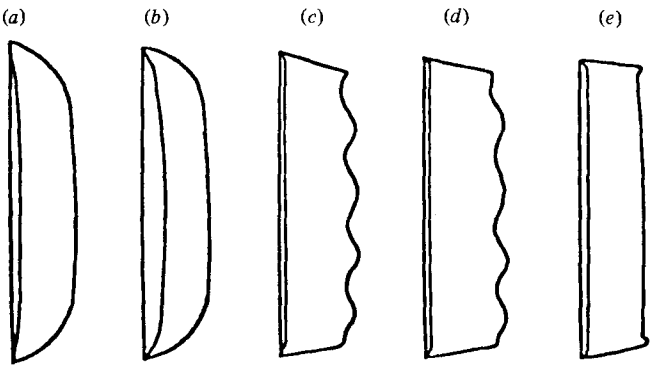

FIGURE 7. Experimental axial-velocity profiles along the vertical centreline of a rotating channel (Hart 1971): (*a*) $\Omega = 0$, (*b*) $\Omega > 0$, with double-vortex secondary flow; (*c*, *d*) $\Omega > 0$, with roll cells; (*e*) $\Omega > 0$, Taylor–Proudman regime.

range of rotation numbers. For this domain, the observed flow consists of longitudinal roll cells superimposed on an axial velocity profile as shown in figure 2. Although it has not been rigorously proved, there is every reason to believe that the onset of roll cells in a large- (but finite-) aspect-ratio channel also constitutes an instability. As we shall soon see, the results of this study support this belief.

In figure 5, computer-generated contour maps of the secondary-flow streamlines are shown at various times in the development of roll cells for $Re = 248$ and $Ro = 0.047$. It is clear that the fluid motion begins with a double-vortex secondary flow, which stretches into the interior of the channel and then splits eventually into six counter-rotating roll cells which are superimposed on a slightly stretched and asymmetric double-vortex secondary flow (see figure 5*d*). The number of roll cells that appear would, of course, depend on the aspect ratio of the channel. For an aspect ratio of eight, which was used for all the calculations conducted here, the maximum number of roll cells that appeared was six. In figure 6(*a*), the axial velocity profile along the horizontal centreline of the channel is plotted for $Re = 248$ and $Ro = 0.047$. The axial profile in the absence of rotations is shown with a dotted line. It is quite clear that the presence of roll cells has a considerable distortional effect on this velocity profile by leading to a strong asymmetry (i.e. the maximum axial velocity is shifted toward the high-pressure side of the channel), with a substantial reduction in the flow rate. For this case, the ratio of the maximum vertical secondary flow to the maximum axial velocity, given by v_m/w_m, is 0.042, and the ratio of the flow rate in a rotating channel to the flow rate in a stationary channel (with the same pressure gradient), given by Q_r/Q, is 0.924. It should be noted that the maximum axial velocity at the horizontal centreline of the channel is shifted toward the high-pressure side of the channel (i.e. the side farthest from the axis of rotation), since, as shown in figure 5(*d*), the roll cells transport momentum to this side. However, in a channel with a different aspect ratio, the maximum axial velocity may be shifted to the opposite side of the channel. For instance, in a channel with an aspect ratio that allows for the development of eight roll cells, momentum would be transported to the low-pressure side of the channel at its horizontal centreline, which is the opposite of the case presented here.

The axial-velocity profile along the vertical centreline of the channel is shown in figure 6(*b*) for $Re = 248$ and $Ro = 0.047$. While this profile is symmetric, it is nevertheless highly distorted by the presence of roll cells. More specifically, the

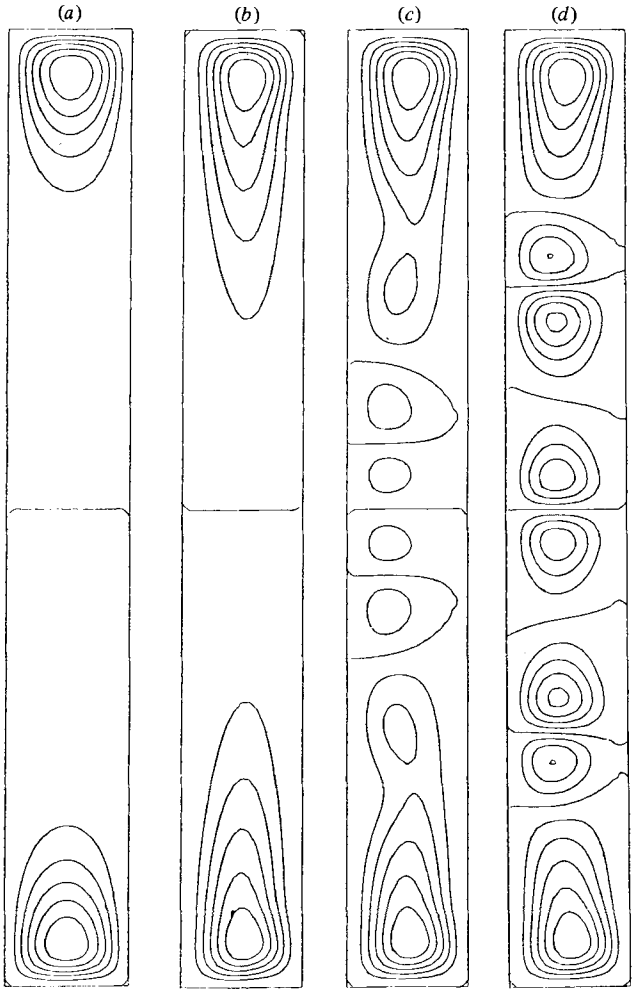

FIGURE 8. Computer-generated secondary-flow streamlines in an 8×1 channel; $Re = 485$, $Ro = 0.014$ ($\Omega = 0.003$ rad/s, $G = 4 \times 10^{-4}$ lb/ft^3): (*a*) $t = 10$ s; (*b*) 400 s; (*c*) 1000 s; (*d*) fully developed.

axial-velocity profile has a distinct wavy structure which is in reasonable qualitative agreement with the experimental observations of Hart (1971) (see figures 7*c*, *d*). The development of roll cells for the case where $Re = 485$ and $Ro = 0.014$ is shown in figure 8. Again, there is a double-vortex secondary flow early on, which stretches to the interior of the channel and then splits into three pairs of counter-rotating roll cells. However, here the separation distance between each pair of roll cells is greater than in the previous case. As we will see below, this is indicative of the fact that the flow is getting closer to the stability boundary. The axial velocity profiles along the horizontal and vertical centrelines of the channel are shown in figures 9(*a*, *b*) for $Re = 485$ and $Ro = 0.014$. As in the previous case, the maximum axial velocity along the horizontal centreline of the channel is shifted to the high-pressure side of the channel, and the axial-velocity profile along the vertical centreline of the channel has a wavy structure. Again, there is a discernible reduction in the flow rate which is of the order of 10%.

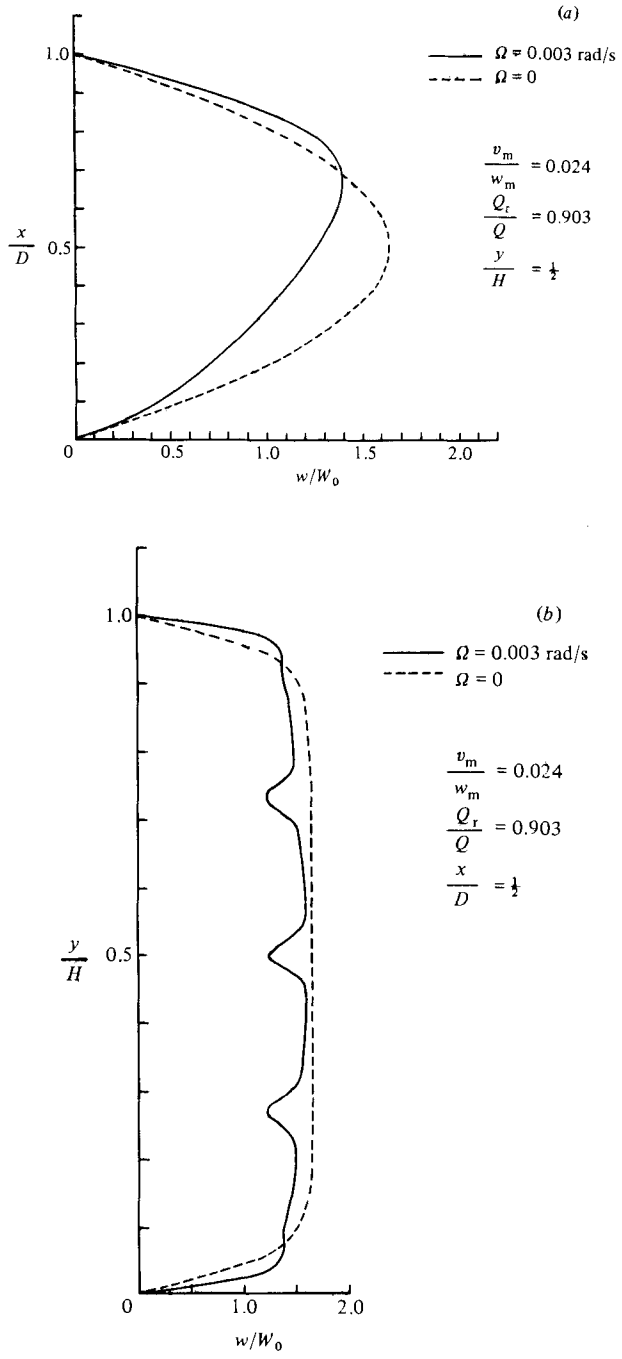

FIGURE 9. Axial-velocity profiles in an 8×1 channel; $Re = 485$, $Ro = 0.014$ ($\Omega = 0.003$ rad/s, $G = 4 \times 10^{-4}$ lb/ft^3): (*a*) along the horizontal centreline of the channel; (*b*) along the vertical centreline of the channel.

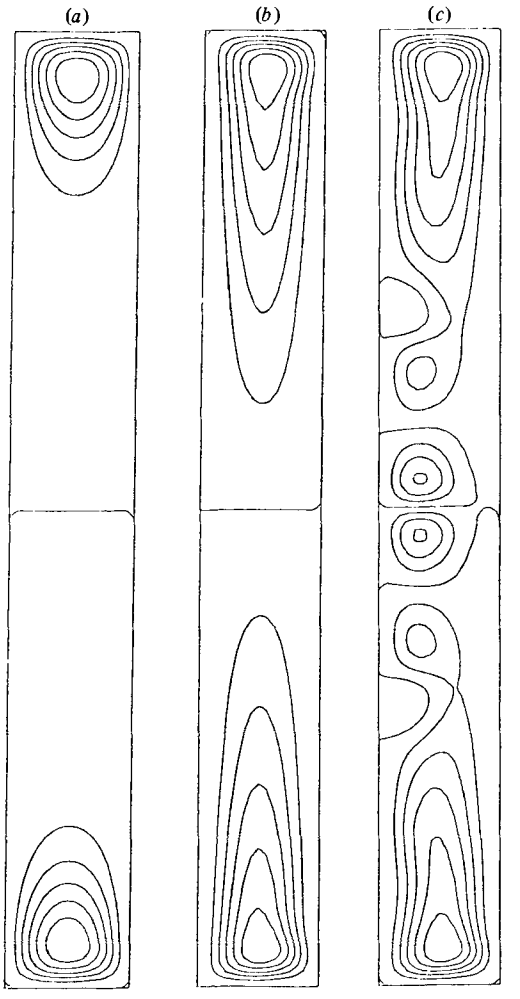

FIGURE 10. Computer-generated secondary-flow streamlines in an 8×1 channel; $Re = 114$, $Ro = 0.514$ ($\Omega = 0.0251$ rad/s, $G = 10^{-4}$ lb/ft^3): (*a*) $t = 10$ s; (*b*) 1500 s; (*c*) fully developed.

Substantial increases in the rotation rate lead to a restabilization of the flow to a Taylor–Proudman regime (i.e. the disappearance of the roll cells). This phenomenon is predicted by Rayleigh's stability criterion, which states that a necessary condition for an instability is that the square of the absolute circulation about the axis of rotation decreases with an increase in the radial distance. Obviously, if the channel is rotated fast enough, the absolute circulation will be dominated by the rotation, which will cause the circulation to increase with an increase in the radial distance. Consequently the flow will become stable. Of course, in the presence of viscosity, this restabilization will occur at lower angular velocities than those predicted by Rayleigh's criterion.

Computer-generated contour maps of the streamlines are shown in figure 10 at various times for $Re = 114$ and $Ro = 0.514$ ($\Omega = 0.0251$ rad/s). It is clear from this figure that the roll cells are starting to weaken. An additional increase in the rotation rate to $\Omega = 0.08$ rad/s (while maintaining the same pressure gradient G) yields a fully restabilized flow where $Re = 107$ and $Ro = 1.75$. The time evolution of the secondary-

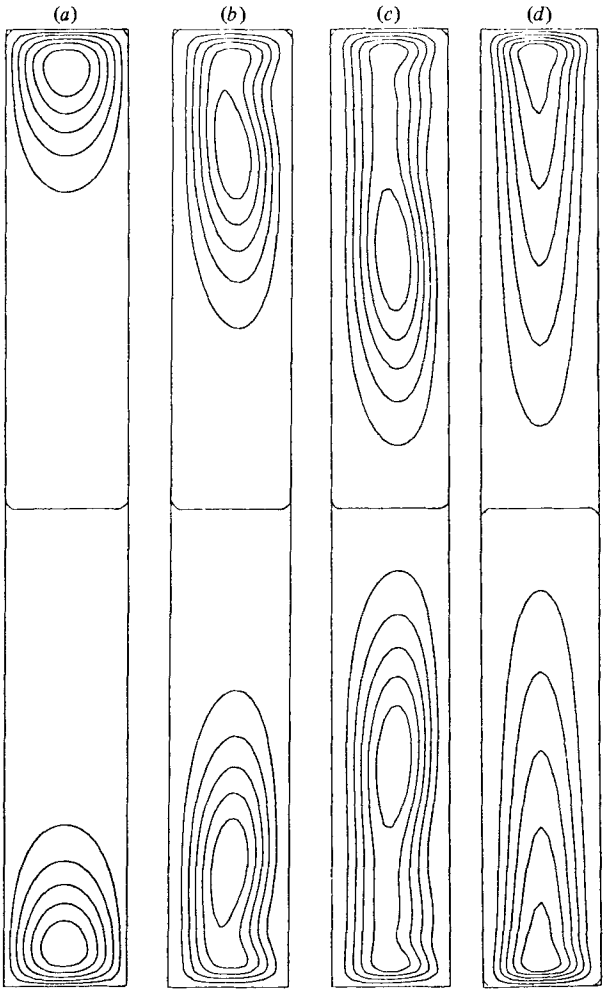

FIGURE 11. Computer-generated secondary-flow streamlines in an 8×1 channel; $Re = 107$, $Ro = 1.75$ ($\Omega = 0.08$ rad/s, $G = 10^{-4}$ lb/ft^3): (*a*) $t = 1$ s; (*b*) 30 s; (*c*) 50 s; (*d*) fully developed.

flow streamlines of this restabilized flow is shown in figure 11. The fully developed secondary flow consists of a stretched double-vortex configuration similar to that shown in figure 4 where each vortex is strongly compressed against the horizontal wall of the channel to which it is adjacent (see figure 11*d*). In figure 12(*a*) the axial-velocity profile along the horizontal centreline of the channel for this case is shown. It is quite clear that the secondary flow leads to a distortion of this profile, with a substantial reduction in flow. More specifically, the axial velocity along the horizontal centreline of the channel is asymmetric, with its maximum velocity shifted toward the low-pressure side of the channel. This results from the fact that the secondary flow near the horizontal centreline of the channel transports momentum toward the low-pressure side of the channel (see figure 11*d*). The axial-velocity profile along the vertical centreline of the channel is shown in figure 12(*b*). It assumes a Taylor–Proudman configuration (i.e. does not vary along the axis of rotation) in the interior of the channel, with the exception of two peaks which are located near the upper and lower walls of the channel. These result from the fact that, at more rapid

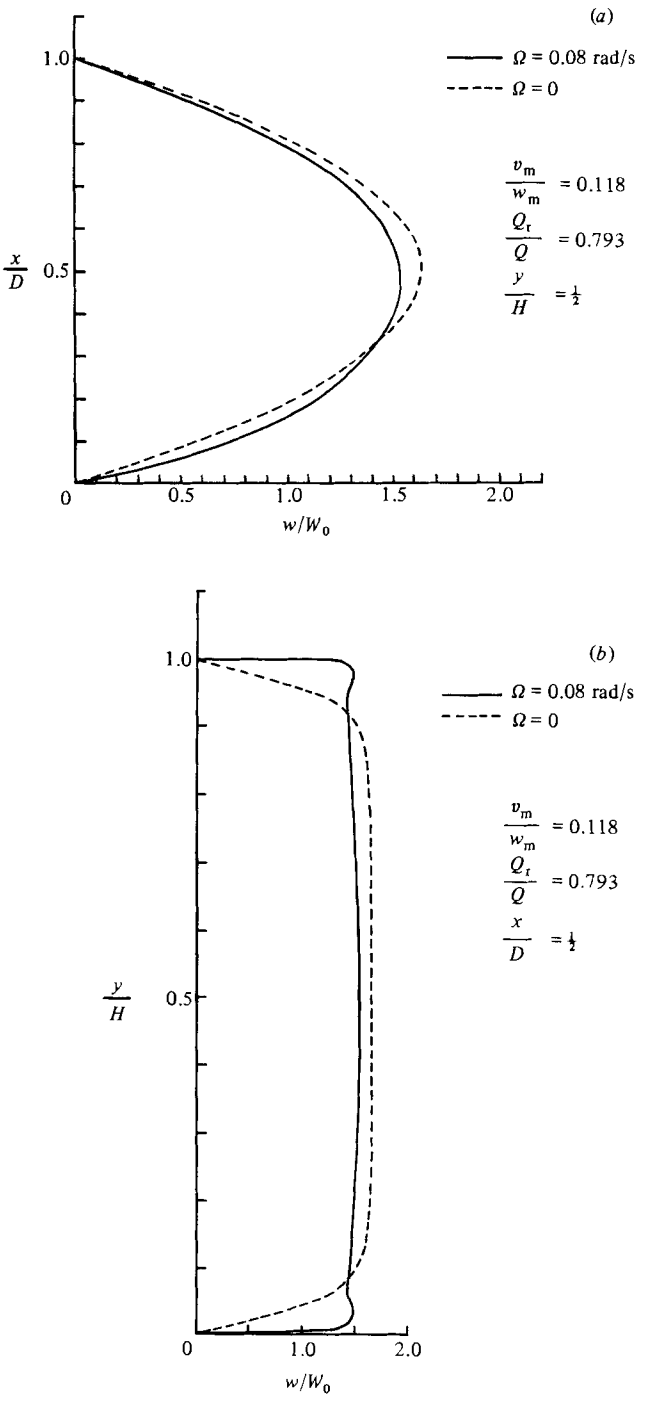

FIGURE 12. Axial-velocity profiles in an 8×1 channel; $Re = 107$, $Ro = 1.75$ ($\Omega = 0.08$ rad/s, $G = 10^{-4}$ lb/ft^3): (*a*) along the horizontal centreline of the channel; (*b*) along the vertical centreline of the channel.

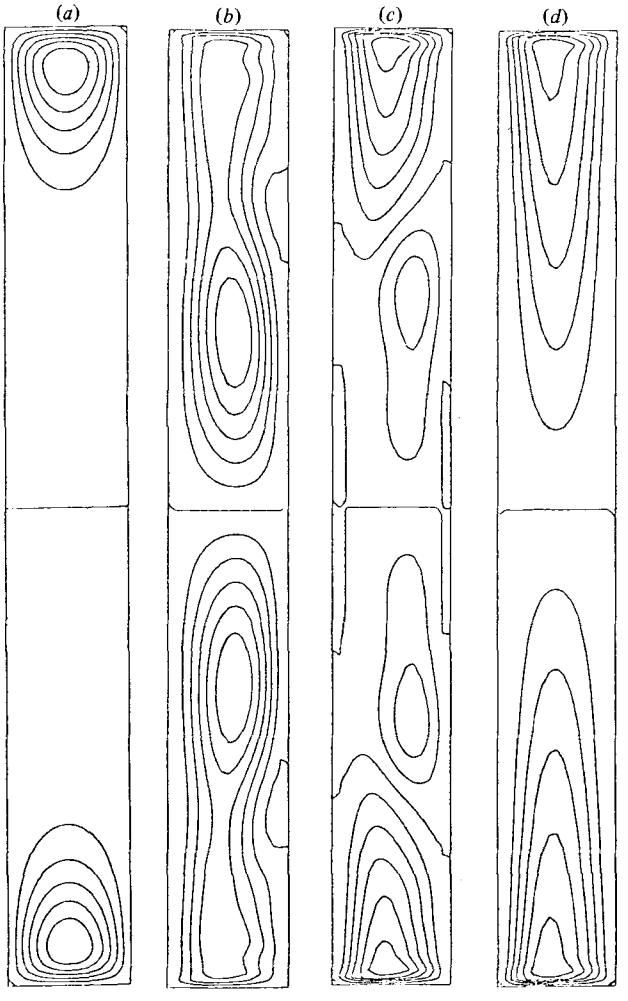

FIGURE 13. Computer-generated secondary-flow streamlines in an 8×1 channel; $Re = 171$, $Ro = 2.73$ ($\Omega = 0.2$ rad/s, $G = 2 \times 10^{-4}$ lb/ft^3): (*a*) $t = 1$ s; (*b*) 25 s; (*c*) 50 s; (*d*) fully developed.

rotation rates, the secondary flow can be thought of as originating from Ekman suction, as discussed in Hart (1971). The numerical results shown in figure 12(*b*) are thus in good qualitative agreement with the experimental observations of Hart (1971) shown in figure 7(*e*). Another set of calculations in the Taylor–Proudman regime are shown in figures 13 and 14 for $Re = 171$ and $Ro = 2.73$ ($\Omega = 0.2$ rad/s). This restabilized flow corresponds to the same pressure gradient as the unstable flow shown in figure 5, and is obtained by simply increasing the angular velocity from $\Omega = 0.005$ rad/s to $\Omega = 0.2$ rad/s. The fully developed secondary flow again consists of a stretched double-vortex configuration (see figure 13*d*), and the axial-velocity profile along the horizontal centreline of the channel is asymmetric, with its maximum velocity shifted toward the low-pressure side of the channel as shown in figure 14(*a*) (there is also a substantial reduction in the flow rate). The axial-velocity profile along the vertical centreline of the channel for this case (see figure 14*b*) assumes a Taylor–Proudman configuration in the interior of the channel, with two peaks located at the upper and lower walls of the channel which arise from Ekman suction

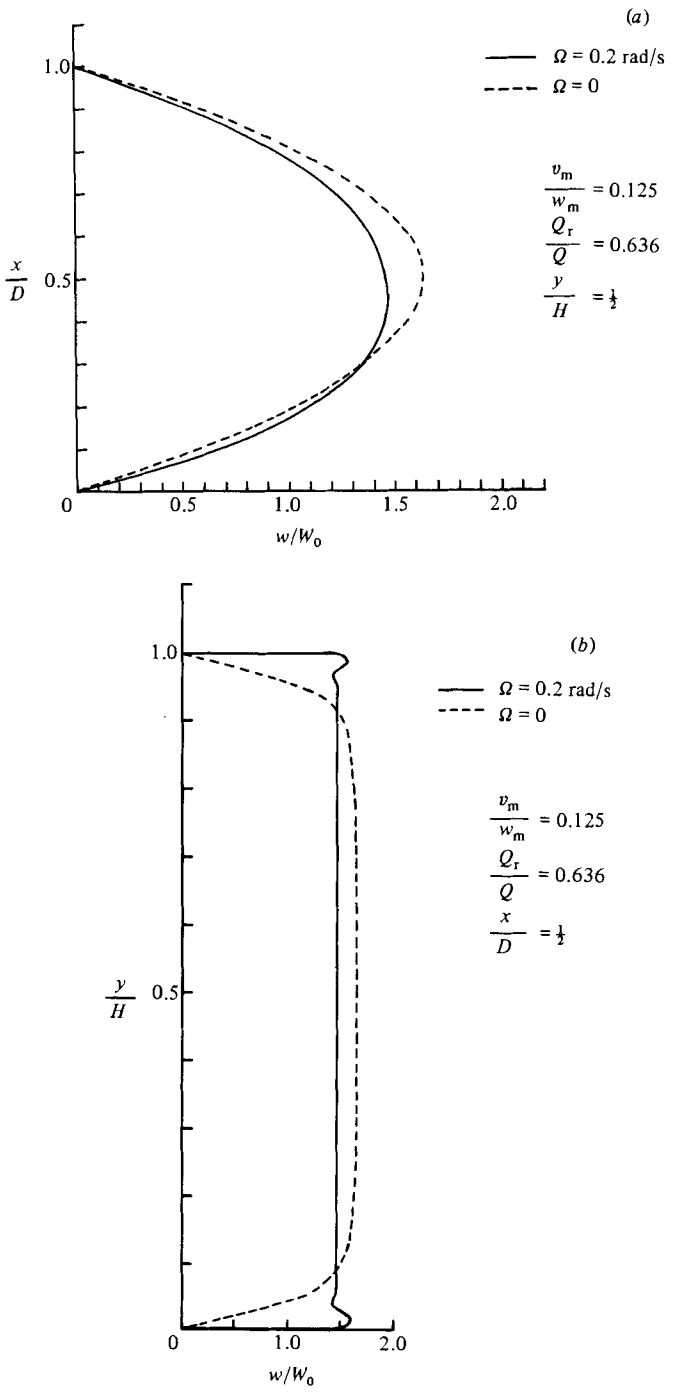

FIGURE 14. Axial-velocity profiles in an 8×1 channel; $Re = 171$, $Ro = 2.73$ ($\Omega = 0.2$ rad/s, $G = 2 \times 10^{-4}$ lb/ft^3): (*a*) along the horizontal centreline of the channel; (*b*) along the vertical centreline of the channel.

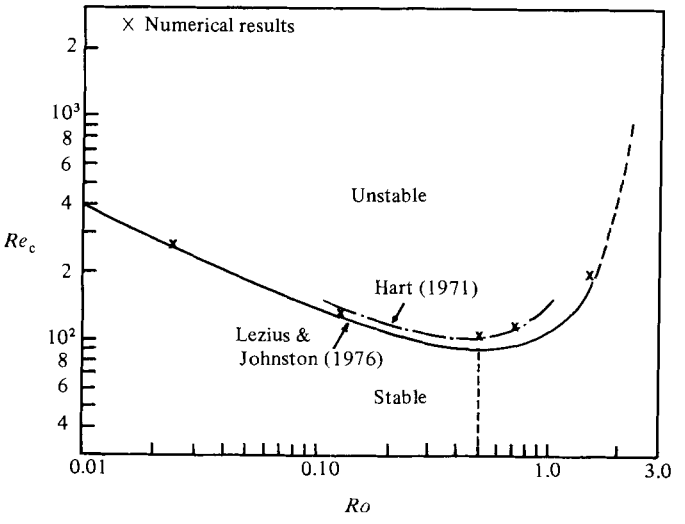

FIGURE 15. Numerically obtained stability-boundary points for the onset of roll-cell instabilities in rotating channel flow.

as discussed previously. This velocity profile is in excellent qualitative agreement with the experimental observations of Hart shown in figure 7(*e*).

The location of the overshoot peaks in figures 12(*b*) and 14(*b*) occur respectively at distances of $y/H = 0.0235$ and $y/H = 0.0156$ from the top and bottom walls of the channel. These results are in the range of values $y/H = 0.0130$ and $y/H = 0.00819$ which are obtained from the linear theory of the Ekman layer using the equation (see Hart 1971)

$$\frac{y}{H} = 2E^{\frac{1}{2}}\frac{D}{H}. \tag{3.2}$$

The difference in these results can be attributed to the fact that the Rossby numbers (i.e. $\frac{1}{2}Ro^{-1}$) for these flows are not extremely small. The Rossby numbers for the results shown in figures 12(*b*) and 14(*b*) are respectively 0.285 and 0.183. In order for (3.2) to be valid, the Rossby number must be much less than unity. Consequently the nonlinear convective terms cannot be entirely neglected in our case as is done in the linear Ekman-layer theory. On physical grounds we would expect the convective terms to transport momentum away from the channel walls, thus leading to the movement of the overshoot peaks to a distance further from the walls, which is in qualitative agreement with these computations.

The numerically obtained stability boundary points are plotted in figure 15 alongside the theoretical results of Hart (1971) and Lezius & Johnston (1976), which were obtained from a linear stability analysis. These results tend to be in excellent agreement with those of Hart near the critical point, whereas away from the critical point they are in excellent agreement with the results of Lezius & Johnston. In particular, we obtained a critical point with the values $Re_c = 110$ and $Ro_c = 0.5$, which are somewhat higher than the values of $Re_c = 88.53$ and $Ro_c = 0.5$ obtained by Lezius & Johnston. However, it should be noted that since our calculations are for a finite-aspect-ratio channel (unlike those of Hart and Lezius & Johnston, which deal with Poiseuille flow) higher stability limits would be expected on physical grounds. More specifically, the presence of the upper and lower walls of channel tend to have a stabilizing effect on the flow. Hence we feel that the results shown in figure

15 are quite encouraging and strongly support the accuracy of the results obtained here. It should be noted at this point that the criterion used to determine the stability boundary points in figure 15 was the appearance of *any* subsidiary vortices in the interior of the channel under steady-state conditions (see e.g. figure 10*c*).

Finally, we would like to make a few comments concerning the role of the nonlinear convective terms in the numerical results presented in this paper. As demonstrated in Speziale (1982), asymmetries in the secondary-flow and axial-velocity profiles have their origin in the convective terms. Consequently, when strong asymmetries occur (cf. figures 9*a*, 10*c*), the convective terms are playing a dominant role. Therefore, in order to understand such effects, the full nonlinear equations of motion must be solved, as has been done here.

4. Summary and conclusion

A detailed numerical study has been conducted of secondary flows and roll-cell instabilities in laminar pressure-driven channel flow subjected to a spanwise rotation. The full nonlinear time-dependent Navier–Stokes equations were solved by a finite-difference method in this study, which, we believe, gives a more complete picture of the physical mechanisms that are manifested in rotating channel flow. At weak rotation rates, a double-vortex secondary flow occurs, consistent with previous studies. More precisely, this secondary flow consists of two counter-rotating vortices, which have a lengthscale of the order of the width of the channel and are somewhat compressed against the upper and lower walls of channel. Of course, this secondary flow has a negligible effect on the axial-velocity profiles at the centerlines of the channel. As the rotation rate is increased for a given axial pressure gradient, this double-vortex secondary flow begins to stretch far into the interior of the channel, where it can have a discernible distortional effect on the axial velocity, with an associated reduction in the flow rate. For $Re > 110$ and $0 < Ro < 3$, an instability occurs in the form of longitudinal roll cells. The numerically obtained critical point of $Re_c = 110$ and $Ro_c = 0.5$ (as well as the other stability boundary points) for the onset of roll cells is within the range of values obtained by Hart (1971) and Lezius & Johnston (1976) by a linear stability analysis. The presence of roll cells were shown to have a severe distortional effect on the axial-velocity profiles. To be specific, the axial-velocity profiles along the horizontal centreline of the channel are asymmetric, with the maximum velocity shifted toward the high-pressure side of the channel, and the axial velocity along the vertical centreline of the channel had a wavy structure, in qualitative agreement with the experimental observations of Hart (1971). There is also a discernible reduction in flow rate for a given axial pressure gradient as a result of the presence of roll cells and secondary flows.

At more rapid rotation rates, the flow restabilizes to a Taylor–Proudman regime. Here the roll cells disappear and a stretched double-vortex secondary flow appears which is quite similar to that which occurs prior to the onset of instability. In the Taylor–Proudman regime there is a considerable distortion of the axial-velocity profiles, with a substantial reduction in the flow rate (for one set of calculations it was of the order of 40 %). The axial-velocity profiles along the horizontal centreline of the channel are asymmetric, with the maximum velocity shifted toward the low-pressure side of the channel, whereas the axial-velocity profile along the vertical centreline of the channel assumes a Taylor–Proudman configuration in the interior of the channel. Peaks in the axial velocity, which arise from Ekman suction, occur at the upper and lower walls of the channel, in agreement with the experimental

observations of Hart (1971). To the best of our knowledge, the calculations presented here represent the first fully nonlinear calculations of roll-cell instabilities and the first complete calculations of the Taylor–Proudman regime in rotating channel flow.

More research is needed to clarify fully the nature of roll-cell instabilities in rotating channel flow. As alluded to earlier, it is most likely that roll-cell solutions exist in parallel with the double-vortex secondary-flow solution for all Re and Ro in a finite-aspect-ratio channel (the double-vortex solution becomes unstable for certain values of Re and Ro). Nevertheless, this should be proven rigorously. Such a proof, which would be difficult because of the three-dimensional structure of the flow, is simply beyond the scope of the present paper. Future research is also needed in the theoretical analysis of turbulent rotating channel flow, which can have important technological applications in the design of turbomachinery. Most of the previous work in this area has tended to be semi-empirical (cf. Majumdar, Pratap & Spalding 1977; Howard, Patankar & Bordynuik 1980) because of the considerable complexity of the flow. In conclusion, there is a wealth of diverse and interesting physical phenomena that occur in rotating channel flow, which, as a result of the research effort of the past decade, are beginning to be better understood.

The authors would like to thank Miss Joanne Fendell for running the computer programs. This work was supported by a grant from the Exxon Education Foundation.

REFERENCES

BATCHELOR, G. K. 1967 *Introduction to Fluid Dynamics*. Cambridge University Press.

BUNEMAN, O. 1969 A compact non-iterative Poisson solver. *Stanford Univ. Inst. for Plasma Research Rep.* SUIPR 294.

HART, J. E. 1971 Instability and secondary motion in a rotating channel flow. *J. Fluid Mech.* **45**, 341–351.

HOWARD, J. H., PATANKAR, S. V. & BORDYNUIK, R. M. 1980 Flow prediction in rotating ducts using Coriolis-modified turbulence models. *Trans. ASME* I: *J. Fluids Engng* **102**, 456–461.

JOHNSTON, J. P., HALLEEN, R. M. & LEZIUS, D. K. 1972 Effects of spanwise rotation on the structure of two-dimensional fully developed turbulent channel flow. *J. Fluid Mech.* **56**, 533–557.

LEZIUS, D. K. 1975 Finite difference solutions of Taylor instabilities in viscous plane flow. *Comp. & Fluids* **3**, 103–110.

LEZIUS, D. K. & JOHNSTON, J. P. 1976 Roll-cell instabilities in rotating laminar and turbulent channel flow. *J. Fluid Mech.* **77**, 153–175.

MAJUMDAR, A. K., PRATAP, V. S. & SPALDING, D. B. 1977 Numerical computation of flow in rotating ducts. *Trans. ASME* I: *J. Fluids Engng* **99**, 148–153.

ROACH, P. J. 1972 *Computational Fluid Dynamics*. Hermosa.

SPEZIALE, C. G. 1982 Numerical study of viscous flow in rotating rectangular ducts. *J. Fluid Mech.* **122**, 251–271.